Polymer Bulletin (2026) 83:499
https://doi.org/10.1007/s00289-026-06562-8

ORIGINAL PAPER

Parametric optimization of silk protein–chitosan core–sheath nanofibers via coaxial electrospinning

Rony Aad[1] · Andrea Hejdová[1] · Ivana Dragojlov[1] · Davide Iaconianni[1] · Simone Mariuzzo[1] · Diletta Ami[2] · Antonino Natalello[2] · Simone Vesentini[1]

Received: 27 February 2026 / Revised: 12 June 2026 / Accepted: 16 June 2026 /
Published online: 26 June 2026

Abstract

Coaxial electrospinning represents a versatile platform for the fabrication of nanofibrous materials with spatially controlled composition and tunable structure–property relationships, broadening their potential across advanced materials applications. In this study, composite nanofibrous films were fabricated from natural biopolymers using a systematically optimised coaxial electrospinning approach. Core–sheath fibres consisting of a silk fibroin (SF) core and a silk sericin (SS)–chitosan (CS) shell were produced through progressive optimisation of solvent systems, blend ratios, and processing parameters. Morphological characterisation by scanning electron microscopy (SEM) demonstrated that fibre diameter, uniformity, and structural integrity were strongly governed by electrospinning configuration and shell composition, with sericin-rich SS: CS blends yielding the most stable and uniform fibres. Transmission electron microscopy (TEM) provided supportive evidence of a core-sheath architecture, revealing distinguishable inner and outer regions within individual fibres. Fourier-transform infrared spectroscopy (FTIR) confirmed the coexistence of all three biopolymers and highlighted composition-dependent differences in molecular organisation. Functional assessment via moisture vapour transmission rate (MVTR) measurements revealed a strong dependence of moisture permeability on electrospun film thickness, with thinner mats exhibiting higher and more stable vapour transmission. Overall, this work establishes the feasibility of producing SF/SS–CS core-sheath nanofibrous scaffolds with controlled morphology, composition, and moisture transport properties through careful process optimisation. Through systematic comparison of spinning configuration, solvent system, and shell composition, this study identifies the critical parameters required for stable and reproducible fabrication of silk-based core–shell nanofibers via coaxial electrospinning.

Keywords Silk fibroin · Silk sericin · Chitosan · Coaxial electrospinning · Biocompatible nanofibers · Sustainable biomaterials

Extended author information available on the last page of the article

Introduction

Electrospinning is a versatile technique for producing nanofibers for various applications [1]. It enables the fabrication of continuous fibres with controlled diameters, high porosity, and tuneable composition [2]. In conventional electrospinning, a polymer solution is stretched into fine fibres under a high electric field and solidifies upon solvent evaporation to form porous nanofibrous membranes [2]. To enhance the functionality of electrospun materials, coaxial electrospinning was introduced as an advanced technique that enables the fabrication of core–sheath nanofibers using a dual-capillary spinneret [3].

Several electrospinning strategies have been developed to fabricate core–sheath nanostructures and related compartmentalized fibrous architectures. In addition to conventional coaxial electrospinning, recent studies have demonstrated the fabrication of fibres with gradient polymer distributions and spatially controlled architectures, enabling enhanced control over material composition and performance [4]. Similarly, gradient distributions of active compounds have been achieved within core–sheath fibres, providing opportunities for precise regulation of encapsulation and release behaviour [5]. More advanced approaches, such as modified triaxial electrospinning, further expand the design flexibility of electrospun materials and have recently been explored for one-step batch fabrication of complex functional nanofibres [6]. Emulsion electrospinning represents an alternative approach for producing core–sheath-like fibres through phase separation within an emulsion, although the resulting internal structures are generally less precisely controlled than those obtained by coaxial electrospinning [7].

Despite these developments, coaxial electrospinning remains one of the most versatile and widely adopted approaches for producing well-defined core–sheath fibres because it enables direct and reproducible spatial separation of materials while allowing independent control of core and sheath compositions. This capability is particularly advantageous when combining biopolymers with distinct solvent requirements and physicochemical characteristics, making coaxial electrospinning especially suitable for the development of multifunctional biopolymer-based nanofibrous systems.

In coaxial electrospinning, the formation of a stable compound jet is essential for achieving a well-defined core–sheath architecture. Under an applied electric field, a stable coaxial jet is formed in which the sheath solution carries the electrical charge while interfacial shear forces elongate the core polymer, resulting in uniform core–sheath fibres after solvent evaporation [8, 9]. This architecture is particularly advantageous, as it allows encapsulation and protection of agents in the core, while the outer sheath provides mechanical support and controlled surface characteristics. The incorporation of multiple materials within a single fibre enables independent tailoring of physicochemical, mechanical, and surface properties [10–12].

Successful coaxial electrospinning is governed by multiple interacting parameters that can generally be grouped into three categories: (i) properties of the working fluids, including polymer concentration, viscosity, conductivity, surface tension, solvent volatility, and compatibility between core and sheath solutions; (ii) operational parameters, such as applied voltage, core and sheath flow rates, needle geometry, and tip-to-collector distance; and (iii) ambient conditions, including temperature

and relative humidity [13]. These factors collectively influence jet stability, solvent evaporation, core–sheath integrity, fibre morphology, and the overall success of the electrospinning process [14]. Because the present work combines SF, SS, and CS using different solvent systems within a coaxial configuration, systematic optimisation of these parameters was necessary to achieve stable fibre formation and well-defined core–sheath structures. Recent reviews have further emphasized that successful coaxial electrospinning requires consideration of the interactions among these parameter groups rather than independent optimisation of individual variables, particularly when combining polymers with different rheological and solvent characteristics [15].

Because these parameters become particularly important when combining biopolymers with different physicochemical and solvent characteristics, the present study employs coaxial electrospinning to fabricate nanofibrous membranes by integrating silk fibroin (SF), silk sericin (SS), and chitosan (CS). The central hypothesis is that a core–sheath architecture comprising an SF core and an SS–CS shell can synergistically combine mechanical stability with tunable surface and structural characteristics within a single fibrous system. SF was selected for the core due to its well-defined secondary structure and excellent mechanical properties, which contribute to the structural stability of the resulting fibres [16–18]. The shell was designed using SS, a silk industry by-product with hydrophilic and cell-interactive properties [19–21], combined with CS, a natural polysaccharide widely recognized for its antimicrobial, structural reinforcement capability, and biodegradable characteristics [22–24]. Previous studies on chitosan-based core–sheath electrospun nanofibers have further shown that chitosan-containing shell layers contribute to improved structural stability and fibre integrity [25, 26].

The rationale for this architecture lies in the complementary functions of the selected biopolymers. SF was positioned in the core to provide mechanical support, whereas the SS–CS outer layer was intended to govern the surface characteristics and interfacial behaviour of the fibres. Beyond its functional advantages, this material strategy also aligns with circular economy principles through the valorisation of sericin, a silk industry by-product, into a high-value functional material.

The sericin used in this study was obtained through a high-temperature high-pressure (HTHP) degumming process that employs only pure water, making the extraction route entirely chemical-free. At the same time, it is acknowledged that the solvent systems required for electrospinning, necessary to achieve stable jets and uniform fibre formation, are not environmentally benign. At present, however, these solvents remain essential for reliable electrospinning of the selected biopolymers, as milder or greener alternatives do not yet provide comparable process stability or material performance.

To test the hypothesis, a systematic experimental design was adopted, involving controlled comparisons between single and coaxial electrospinning, different solvent systems, and systematic variation of the SS: CS ratio in the shell, ranging from equimolar (1:1) to sericin-rich (3:1) compositions, to assess the influence of shell composition on processability and fibre morphology. These comparisons directly probe the necessity of architectural separation, solvent compatibility, and shell composition in achieving stable and reproducible core–sheath architectures. This study therefore

identifies the key processing parameters required for stable and reproducible fabrication of SF/SS–CS core–sheath nanofibers, establishing clear process–structure relationships within this multi-component coaxial system.

Materials and methods

Materials

Bombyx mori silk cocoons were supplied by the Council of Research in Agriculture and Analysis of Agricultural Economics (CREA, Padua, Italy). Trifluoroacetic acid (TFA, ≥99% purity) was purchased from Tokyo Chemical Industry Co. (TCI). Formic acid (FA, 98–100% purity) and calcium chloride ($CaCl_2$) were obtained from SAFC (Sigma-Aldrich Fine Chemicals). Chitosan (Thermo Fisher Scientific / Acros Organics, CAS 9012-76-4) with a degree of deacetylation≥75% and a molecular weight of 100–300 kDa was used. Consumables used for electrospinning, including Luer-lock syringes, polypropylene (PP) male and female Luer-lock connectors, uni- and coaxial stainless-steel Luer-lock syringe needles (ranging in diameter from 30G to 10G), and Tygon/PTFE tubes, were procured from Colaver s.r.l. (Monza, Italy).

Silk fibroin (SF) and sericin (SS) extraction and purification

SF and SS were extracted and purified from *Bombyx mori* cocoons at Leonardino s.r.l. (Bollate, Milan, Italy) using a high-temperature high-pressure (HTHP) degumming process. A total of 60 g of cocoons were manually opened to remove the pupae, then placed in crystallizing dishes containing 800 mL of distilled water. Each dish was covered with a glass Petri dish and inserted into autoclave bins. The degumming was conducted in an Asal Vapormatic 770 autoclave at 121 °C and 15 psi for 60 min. Post-degumming, the aqueous sericin-rich solution was separated from the remaining fibroin fibres by filtration using Fisherbrand™ glass funnel filters with sintered glass discs. The sericin solution was processed into powder using a Shanghai Pilotech YC-015 spray dryer. Spray-drying was performed with an inlet temperature of 120 °C, outlet temperature of 70 °C, and airflow rate of 4.5 m^3/h. The resulting high-purity sericin powder was stored in airtight containers at room temperature for further use. Meanwhile, the fibroin-rich material, separated after degumming, was washed six times in 1.5 L of distilled water at 90 °C, manually squeezed and stretched to remove residual sericin, and then dried overnight in a laminar flow hood. The dried skeins were carded manually to produce uniform fibre bundles. Fibroin was dissolved in a 2% w/v calcium chloride/formic acid solution to prepare an 8% w/v fibroin solution. After 90 min of stirring at 600 rpm under a fume hood, the solution was vacuum filtered to remove undissolved residues. SF films were prepared by solvent casting 5 mL of the filtered solution into plastic Petri dishes, followed by drying at room temperature, water rinsing, and redrying. The resulting SF films, together with SS powder, were subsequently used in the electrospinning process to fabricate composite nanofibrous films. Solvent-cast SF films are generally reported to retain a significant proportion of Silk I and random-coil conformations, with limited forma-

tion of the more ordered Silk II β-sheet structure. Consequently, these films typically exhibit lower crystallinity than post-treated fibroin materials in which β-sheet formation has been intentionally induced. However, in the present work, the solvent-cast films served solely as an intermediate material for storage and handling prior to their subsequent dissolution in FA for electrospinning. Therefore, the structural and degradation properties of the cast films themselves were not expected to directly determine the properties of the final electrospun fibres [16, 17, 27, 28].

More generally, the molecular conformation of silk proteins is known to be strongly influenced by both extraction conditions and subsequent dissolution in electrospinning solvents. The extraction and recovery procedures used for silk proteins can alter molecular organisation, aggregation state, and intermolecular interactions, leading to conformational changes that may subsequently influence electrospinning behaviour. SF contains highly ordered crystalline regions associated with β-sheet-rich Silk II structures [29], whereas SS is generally characterized by a greater proportion of amorphous and random-coil conformations [30]. These intrinsic structural differences contribute to the distinct physicochemical behaviour of SF and SS and provide additional context for understanding their behaviour during dissolution and electrospinning.

Preparation of sericin, fibroin, and chitosan solutions for electrospinning

The solubilization of SS, SF, and CS for electrospinning required careful selection of solvents to ensure compatibility and stability of each component. Due to limitations of the coaxial setup, which allows a maximum of two solvent systems, TFA was selected to dissolve both SS and CS, while FA was used to dissolve SF. These choices were based on the solubility characteristics of the materials and previous reports regarding their behaviour in acidic electrospinning solvents.

FA and TFA are fully miscible polar organic acids and have both been widely employed as solvents for silk-based electrospinning systems [31]. Their mutual miscibility is advantageous in coaxial electrospinning because it reduces the likelihood of macroscopic phase separation at the core–sheath interface and facilitates formation of a stable compound jet. This compatibility was an important consideration in the present work, as it enabled the use of FA-based core solutions and TFA-based shell solutions within the same coaxial process without evident interfacial instability. However, solvent miscibility alone does not guarantee identical electrospinning behaviour. FA and TFA differ in volatility, acidity, and their interactions with silk proteins, which can influence solvent evaporation rates, protein conformation, jet stability, and ultimately fibre morphology. Therefore, although the FA/TFA solvent pair was considered compatible from a processing perspective, optimisation of the electrospinning parameters remained necessary to accommodate solvent-specific effects on fibre formation and process stability.

Dissolution in strong organic acids disrupts intermolecular hydrogen bonding and can alter protein secondary structure; in particular, TFA has been reported to promote conformational disruption and increased random-coil content in silk fibroin, whereas FA is generally regarded as a milder solvent that better preserves fibroin structural organization during processing [32]. These solvent-dependent structural differences

may contribute to differences in electrospinning behaviour and fibre morphology by influencing intermolecular interactions within the spinning solution.

The evaporation behaviour of these solvents also influences electrospinning parameters. FA possesses a slightly higher vapour pressure (~44 mmHg at 25 °C) and is therefore often processed using shorter tip-to-collector distances than TFA in single-solution electrospinning. However, all coaxial experiments in the present study were conducted using a fixed tip-to-collector distance of 15 cm. This value was selected during the optimisation stage because the coaxial configuration requires a single working distance and applied voltage for both the core and sheath solutions. A distance of 15 cm provided sufficient solvent evaporation for both the FA-based core and the TFA-based sheath solutions prior to fibre collection while maintaining stable jet formation across all coaxial formulations.

SF solution was prepared by dissolving 4 g of calcium chloride (2% w/v) in 200 mL of FA, followed by the addition of 16 g of SF films (8% w/v). The mixture was stirred at 400 rpm until salts were dissolved, then at 600 rpm for 1.5 h to fully solubilize the fibroin. The solution was vacuum filtered to remove any undissolved residues. SS and CS powders were weighed and gradually added to the desired volume of TFA under a fume hood. Each solution was stirred using a magnetic stirrer until fully dissolved, with solubilization times adjusted based on concentration and material type. For SS and CS, solutes were gently added to prevent premature gelling. The final solutions were stored in sealed containers and used immediately in the coaxial electrospinning process.

Electrospinning process

Work plan and electrospinning strategy

This study followed a stepwise and hierarchical approach to electrospinning, beginning with the individual optimization of each biopolymer, SS, SF, and CS, to establish well-defined and reproducible electrospinning windows. For each polymer, the most suitable solvent, concentration (wt%), applied voltage (ΔV), flow rate (Q), and working distance were determined to achieve stable jet formation and continuous fibres. These preliminary optimizations were essential for establishing experimental control and ensuring reproducibility before increasing system complexity. Once the optimal conditions were identified for each single-polymer solution, the work progressed to coaxial electrospinning, representing a controlled transition from homogeneous systems to heterogeneous core–sheath architectures. This stage involved combining materials in core–sheath configurations, with explicit consideration of solvent compatibility, concentration balance, and parameter matching between core and shell solutions to maintain system stability and prevent jet breakup. The overall experimental strategy is illustrated in Fig. 1, which provides a three-dimensional schematic visualization of the electrospinning plan rather than experimental data. In this representation, the axes correspond to the solute concentrations (wt%) of SS, SF, and CS, defining the compositional space explored in the study, while the horizontal planes represent different electrospinning configurations, distinguishing single-material systems from core-sheath pairings. Coloured squares indicate individual

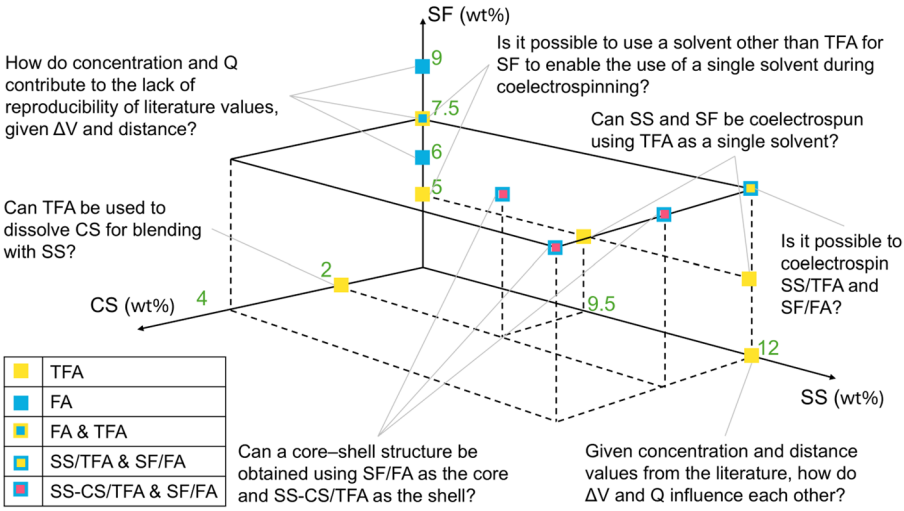

Fig. 1 Three-dimensional schematic representation of the stepwise electrospinning strategy employed in this study. The diagram maps the progressive transition from single-material electrospinning to core–sheath configurations within a defined compositional space. Axes represent solute concentrations (wt%) of silk sericin (SS), silk fibroin (SF), and chitosan (CS). Horizontal planes correspond to distinct electrospinning configurations, including single-polymer systems and coaxial pairings. Coloured squares indicate individual experimental conditions, each representing a specific combination of polymer composition, solvent system, and electrospinning parameters (ΔV, Q, working distance). The figure illustrates how individual polymer optimization informed the selection of stable core-sheath architectures investigated in this work

experimental conditions, with each square corresponding to a unique combination of polymer composition, solvent system, and electrospinning parameters. The figure explicitly illustrates the logical progression from single-polymer optimization (SS/TFA, SF/FA, SF/TFA, and CS/TFA) toward increasingly complex core-sheath systems, including SS/TFA–SF/FA, SS/TFA–SF/TFA, and SS–CS/TFA–SF/FA. This visualization clarifies how successful single-material optimization guided the selection of viable core–sheath pairings and highlights the exclusion of unstable or incompatible combinations. After selecting the most relevant systems for the objectives of the study, detailed SEM analyses were performed to evaluate fibre morphology, focusing specifically on fibre diameter. For these selected systems, ΔV and Q were further refined to minimize diameter dispersion and promote uniform, defect-free fibres. Images were processed using Phenom Pro Suite software, enabling quantitative fibre diameter analysis. The samples that exhibited the most uniform fibre distribution, continuous structures, and the smallest diameters were considered the most suitable to proceed with.

Electrospinning sample preparation

Tygon tubing was cut to slightly exceed the distance between the syringe pump and spinneret plate, with male and female connectors attached to each end. The syringe was connected to the tubing via the female connector. Under a fume hood, the plunger

was removed, and the polymer solution was carefully loaded into the syringe, filling approximately 70–80% of its volume to minimize air bubbles. The plunger was partially reinserted, and the syringe was inverted to expel air by pushing the plunger until the solution fully occupied the tubing. The needle was then connected to the tubing through the male connector. The needle was inserted into the spinneret orifice and secured with the positively charged electrode, stabilized with tape. A protective paper sheet was placed beneath the needle to prevent contamination. The syringe assembly was placed in the pump holder of the electrospinning machine. The pump was activated to deliver the solution at the set flow rate. The machine doors were closed, and voltages were applied, with the needle positively charged and the collector grounded. The Taylor cone formation was monitored via an external display, and electrospinning was conducted for at least 30 min to deposit fibres onto aluminium foil collectors. Flow rates and voltage were adjusted as needed to maintain stable fibre formation and avoid clogging. After completion, voltage and flow were stopped, the fibre mats removed, and samples prepared for further analysis. Electrospinning was performed under controlled environmental conditions, with temperature maintained at 22–25 °C and relative humidity at 35–40% RH, which remained constant throughout all experiments to ensure reproducibility. For single-needle spinning of SS/TFA and CS/TFA solutions, 15G stainless-steel needles were used to provide a sufficiently large inner diameter and minimize clogging of the highly viscous solutions. For coaxial spinning, 22G (core) and 18G (shell) concentric needles were employed. The narrow annular space between the needles necessitated a reduction in flow rates compared to the single-needle setup to maintain a stable jet. The coaxial needles were mechanically assembled by screwing; however, the exact protrusion length of the inner needle and the concentric alignment of the capillaries were not actively measured or adjusted.

Standard electrospinning: Single-material optimization

The standard electrospinning process was conducted using the three biopolymers: SS, SF, and CS. All solutions were prepared by dissolving the solutes in 10 mL of solvent at concentrations chosen to achieve optimal electrospinning performance. For SS dissolved in TFA, a concentration of 12 wt% was selected based on optimization, as higher concentrations (16–21 wt%) reported in the literature were too viscous and unmanageable, while concentrations below 12 wt% resulted in droplet formation on the samples [33]. The solution was stirred at 150 rpm for 3 h at room temperature. Electrospinning was performed using a 15G needle, with a 15 cm tip-to-collector distance, applied voltages ranging from 20 to 29 kV, and flow rates between 0.25 and 3 mL/h. For SF dissolved in FA, three concentrations (6, 7.5, and 9 wt%) were tested. These solutions required only 30 min of stirring at 150 rpm, at room temperature, and were electrospun using a 17G needle, with voltages between 22 and 26 kV, flow rates from 0.4 to 1 mL/h, and tip-to-collector distances of 12–15 cm. SF solutions in TFA at 5 wt% and 7.5 wt% were also prepared, requiring 3 h of stirring at 150 rpm, at room temperature, and tested under voltages from 15 to 27 kV, flow rates between 0.2 and 0.8 mL/h, and a 15 cm tip-to-collector distance, also using a 17G needle. For CS dissolved in TFA at 2 wt%, the solvent was preheated to 45 °C before gradually

adding the powder under stirring at 400 rpm. After complete dissolution (~ 30 min), the solution was left to set for 2.5 h. The chitosan (CS) solution in trifluoroacetic acid (TFA) required a setting period to ensure stable electrospinning. After solubilization at 45 °C, the solution was allowed to rest for 2.5 h to stabilize viscosity. This step is essential because CS markedly increases viscosity through intermolecular network formation; sufficient setting time ensures stable rheological properties, enabling continuous jet formation and uniform fibres. Electrospinning parameters were selected based on both the literature [34] and additional optimization. Voltages ranged from 18 to 32 kV, flow rates from 0.3 to 2 mL/h, with a 15 cm tip-to-collector distance, using a 15G needle. All the different single-material electrospun samples under varying parameters are listed in the Supplementary document.

Coaxial electrospinning: Core (SF) and shell (SS-CS blend) optimization

Coaxial electrospinning was performed using concentric needles (inner/core: 22G; outer/shell: 18G) with combinations SS and SF or SS and CS dissolved in different solvent systems (FA or TFA). Each solution was prepared in 10 mL of solvent at concentrations determined from the standard electrospinning optimization. Stirring times were 3 h at 150 rpm for SS, 30 min for SF in FA, 3 h for SF in TFA, and CS was stirred at 400 rpm with initial heating. Selected concentrations were SS/TFA (12 or 9.5 wt%), SF/FA (7.5 wt%), SF/TFA (5 wt%), and CS/TFA (2 or 4 wt%). SS and CS were blended in volume ratios of 1:1 or 3:1, followed by an additional hour of stirring to ensure homogeneity. In the single-pump setup, syringes operated at matched flow rates between 0.015 and 0.5 mL/h under fixed voltages of 26 or 29 kV. The dual-pump configuration allowed independent flow rate control from 0.015 to 0.2 mL/h, with voltages up to 32 kV. All experiments maintained a 15 cm tip-to-collector distance. Coaxial electrospinning parameters were optimized to produce core-sheath fibres with stable morphology and solvent compatibility. Environmental conditions were strictly controlled, with temperatures maintained between 22 and 25 °C and relative humidity between 35 and 40%, in line with literature recommendations for reproducible electrospinning [35]. All the different coaxial electrospun samples under varying parameters are listed in the Supplementary document.

Characterization techniques

Morphological characterization of electrospun films by Scanning Electron Microscopy (SEM)

To evaluate the morphological characteristics of the electrospun fibres, Scanning Electron Microscopy (SEM) was employed. This technique enabled qualitative and quantitative assessment of surface morphology, fibre continuity, and structural integrity. Fiber diameter distributions were quantified from SEM micrographs by constructing histograms to evaluate morphological uniformity across samples. SEM imaging was performed using a Phenom XL G2 Desktop SEM (Thermo Scientific), providing a resolution of up to 10 nm and rapid image acquisition. Quantitative fibre diameter measurements were conducted using Phenom ProSuite software.

For each experimental condition, $N = 100$ independent fibre diameter measurements were collected. Structural artifacts such as beads, large droplets, or poorly structured fibres were excluded from analysis to focus on well-formed fibres. Diameter data were exported as single-column vectors (nm) for subsequent statistical analysis.

Data normality and variance homogeneity were assessed using Shapiro–Wilk and Levene's tests, respectively. Given frequent violations of normality, Welch-corrected parametric tests and nonparametric methods were preferentially applied. Multi-group comparisons were conducted using the Kruskal–Wallis test followed by Dunn's post-hoc analysis. For all statistical analyses, differences were considered statistically significant at $p < 0.05$.

For two-group comparisons within the coaxial system, Student's t-tests were used to assess the effect of sericin concentration. Kolmogorov–Smirnov tests were applied to compare distribution shapes, and relationships between processing parameters and fibre diameter were evaluated using Ordinary Least Squares and rank-based regression models.

Morphological characterisation of electrospun films by Transmission Electron Microscopy (TEM)

Transmission Electron Microscopy (TEM) was employed for the investigation of the internal structure of the fibres, especially to verify the presence of a core-sheath configuration in coaxial electrospinning. Sample CHCO7, composed of SS/TFA and CS/TFA (3:1 v/v) mixed with SF/FA, at concentrations of 9.5 wt% SS/TFA, 2 wt% CS/TFA, and 7.5 wt% SF/FA, using a tip-to-collector distance of 15 cm, a flow rate of 0.025 mL/h, and an applied voltage of 29 kV, was electrospun onto copper grids (carbon coated, 300 mesh). TEM micrographs were acquired with JEOL JEM 2100Plus Transmission Electron Microscope (JEOL, Japan) operating with an acceleration voltage of 200 kV and equipped with an 8-megapixel Gatan (Gatan, USA) Rio Complementary Metal-Oxide-Semiconductor (CMOS) camera.

Attenuated Total Reflection Fourier Transform Infrared (ATR-FTIR) Spectroscopy

Fourier Transform Infrared Spectroscopy (FTIR) was employed to analyse the structural properties of the electrospun fibres, with particular focus on identifying characteristic vibrational modes associated with protein secondary structures. Additionally, the technique was used to detect potential residual solvents, particularly trifluoroacetic acid (TFA), by examining signals corresponding to protonated amino groups and salt formations, indicative of solvent–polymer interactions. ATR-FTIR measurements were performed using a Varian 670-IR spectrometer (Varian Australia Pty Ltd., Mulgrave, VIC, Australia) equipped with a nitrogen-cooled mercury cadmium telluride (MCT) detector. Spectra were acquired with a spectral resolution of 2 cm^{-1}, a scan rate of 25 kHz, and 1024 co-added scans using triangular apodization. The attenuated total reflection (ATR) accessory was a single-reflection diamond crystal (Quest, Specac Ltd., Pleasantville, NY, USA), equipped with a pressure clamp that ensures intimate contact between the sample and the crystal. As a result, the acquired absorp-

tion spectra exhibited a flat baseline with no evidence of scattering artifacts [36, 37]. To resolve secondary structure components in the Amide I region, second-derivative spectra were calculated from absorption spectra that had been smoothed using the Savitsky–Golay method and then normalised to the Amide I band area. FTIR data acquisition and processing were performed using Resolutions Pro software (Version 5.4.1.3412, Varian Australia Pty Ltd., Mulgrave, VIC, Australia).

Moisture Vapour Transmission Rate (MVTR) Evaluation

The breathability of the electrospun films was quantified as the Moisture Vapour Transmission Rate (MVTR) using the gravimetric wet cup method in accordance with ASTM E96 guidelines. A humidity gradient was established by maintaining a saturated environment within the test flasks, which were then exposed to a controlled external climate of 37 °C and 90–95% relative humidity in an incubator. The films were securely sealed over the flask opening with double-sided laboratory adhesive tape to prevent any leakage or edge effects. The assembled system was weighed at regular intervals (every 2 h), and measurements continued until a steady-state linear weight loss trend was achieved.

Kinetic data representing mass loss over time were processed in MATLAB for films produced at different durations (30 min, 1 h, and 1.5 h) to determine the steady-state transmission rate. For each film, the mass-loss rate was obtained from linear regression of the weight-loss data as a function of time. The reported 95% confidence intervals correspond to the uncertainty associated with the fitted regression slope and were calculated from the linear regression model for each individual film. These intervals therefore, reflect the goodness of fit of the weight-loss data over time rather than variability between independent film replicates. To ensure the integrity of the slope estimation, particularly for the thicker films where nonlinear instabilities were observed, robust linear regression with Huber weighting was implemented alongside ordinary least-squares (OLS) estimation. This computational approach allowed for the identification and mitigation of suspected outliers, resulting in correlation coefficients (R^2) near unity for the optimized 30-minute and 1-hour samples.

The reliability and repeatability of the fabrication and testing protocols were rigorously validated through a one-way ANOVA followed by Tukey's post-hoc test on four independent replicates of the optimized CHCO7 sample (30-minute electrospinning duration). Furthermore, measurement precision was quantified using the coefficient of variation (CV) at each time point. Finally, to ensure clinical relevance and facilitate benchmarking against existing literature, raw MVTR values were mathematically normalized to a reference relative humidity of 80%. This comprehensive statistical framework ensures that the observed differences in permeability are a direct function of film thickness and composition rather than experimental noise or procedural variability.

Results and discussions

Electrospinning

A key focus of this study was the optimization of electrospinning parameters for the individual biopolymers, SS, SF, CS, with special attention to how solvent choice and processing conditions affected electrospinnability, fibre morphology, and process stability. In the optimization of SS electrospinning using TFA (Table S1), a concentration of 12 wt% was found to yield well-structured fibres. More dilute solutions increased the occurrence of defects due to excess solvent and reduced evaporation, while more concentrated solutions exhibited high viscosity, hindering stable jet formation [33].

Based on these observations, 12 wt% SS/TFA was identified as the most suitable concentration for electrospinning of pure SS solutions. It should be noted, however, that this optimization was performed using SS/TFA solutions alone. In the subsequent coaxial experiments, the shell phase composition differed from the pure SS system and, in some formulations, included chitosan. The chitosan-containing coaxial (CHCO) formulations suggest that the addition of a limited amount of CS can modify the electrospinning behavior of the shell solution and improve fibre morphology and dimensional uniformity. Conversely, excessive CS content increases solution viscosity and may negatively affect fibre quality. Consequently, the optimum concentration identified for pure SS solutions cannot be directly extrapolated to blended SS/CS shell systems used in the coaxial configurations.

Flow rates above 0.75 mL/h led to frequent clogging at the needle's tip, causing instability; this was partially mitigated by increasing the applied voltage to 26 kV. The most uniform fibres, with an average diameter of 800 nm, were produced at a lower flow rate of 0.5 mL/h.

SF behaviour varied significantly depending on the solvent (Table S3). SF dissolved in TFA required longer solubilization times and led to poorly defined fused fibre mats during electrospinning, especially at high concentrations. Reducing the SF/TFA concentration from 7.5 wt% to 5 wt%, combined with a 0.5 mL/h flow rate and 21 kV applied voltage, improved structural integrity but still produced relatively thick fibres (~ 1400 nm). This behaviour may be related not only to solvent evaporation characteristics but also to solvent-induced changes in fibroin molecular conformation. Previous studies have shown that exposure to different solvent systems and subsequent processing treatments can alter fibroin molecular organization and secondary structure, thereby influencing the properties and morphology of electrospun fibres [38]. For example, in electrospun SF/CS systems prepared using TFA-containing solvents, fibroin has been reported to exist predominantly in a random-coil conformation, while subsequent alcohol treatment promotes a transition toward β-sheet-rich structures [39]. These observations suggest that the poorer electrospinning performance observed for SF/TFA formulations may be partly associated with solvent-induced disruption of fibroin molecular organization, which can affect intermolecular interactions, chain entanglement, and jet stability during fibre formation. In contrast, SF dissolved in FA exhibited superior electrospinnability and process versatility (Table S2). Initial trials at 7.5 wt% and 1 mL/h resulted in diameter vari-

ability and imperfections. However, reducing the flow rate to 0.5 mL/h while maintaining a 15 cm working distance and 26 kV voltage led to the formation of uniform nanofibers (~ 400 nm). This combination provided a balance between mechanical integrity and fibre size. These optimized conditions served as the basis for the subsequent coaxial electrospinning experiments, in which SF was selected as the core material and SS as the shell component.

Coaxial electrospinning with different solvents (SS/TFA and SF/FA) required precise tuning of parameters to accommodate the smaller geometry of coaxial needles (Table S5). Voltages were increased to 29–32 kV, and flow rates were reduced to 0.015 mL/h. A dual-pump system allowed fine control over the flow of both core and shell solutions, helping to balance viscosity and prevent jet instability. Conversely, using TFA as a single solvent for both SS and SF exacerbated SF's solubility issues, leading to severe process instability and requiring a reduction in SS concentration (Table S6).

Due to these limitations, the study transitioned to a new shell formulation, a SS-CS blend in TFA, with SF/FA as the core (Table S7). CS presented unique challenges: it required solubilization in TFA at elevated temperatures (45 °C) and low concentrations (2 wt%) to form stable solutions (Table S4). Although standard electrospinning of CS produced fine fibres (~320 nm) at 29 kV and 1 mL/h, blending CS with SS significantly increased viscosity due to strong intermolecular interactions forming three-dimensional networks. To overcome these limitations, the SS concentration was reduced and the SS: CS ratio adjusted to 3:1 (v/v), which enabled stable fibre formation with average diameters of ~450 nm, smaller than SS alone (~800 nm). These findings highlight CS's potential as a fibre-size modifier when used at appropriate ratios without compromising process stability.

Previous studies on electrospun silk fibroin/chitosan systems have reported similar reductions in fibre diameter following the incorporation of moderate amounts of CS, even when solution viscosity increased [31, 40]. This behaviour has been attributed to the ionic nature of chitosan, whose protonated amino groups increase solution conductivity and promote greater electrostatic stretching of the electrospinning jet, resulting in enhanced jet thinning and the formation of finer fibres. At the same time, chitosan incorporation increases solution viscosity, which generally opposes jet stretching and tends to increase fibre diameter. The final fibre morphology therefore depends on the balance between these competing conductivity- and viscosity-related effects. In previously reported SF/CS systems, the reduction in fibre diameter was attributed primarily to conductivity-related effects, which appeared to outweigh the opposing influence of increased viscosity at moderate CS concentrations [31]. Although viscosity and conductivity were not directly measured in the present study, the reduced fibre diameter observed for the SS-CS shell formulations is consistent with these previously reported trends and provides a plausible explanation for the superior dimensional characteristics observed in CHCO7.

Based on the results of these optimisations, eight representative samples were selected for further characterisations; they were the best-performing formulations from each experimental category, chosen for their fibre morphology, fibre diameter, and electrospinning process stability, as reported in Table 1.

Table 1 The eight best-performing samples from the coaxial electrospinning experiments and their corresponding optimal conditions

Sample name	Composition	Concentrations (wt%)	Distance (cm)	Q (ml/h)	ΔV (kV)
CO5	SS / TFA and SF / FA	SS/TFA: 12 SF/FA: 7.5	15	0.025	29
CO6	SS / TFA and SF / FA	SS / TFA: 12 SF / FA: 7.5	15	SS: 0.025 SF: 0.015	29
SCO4	SS / TFA and SF / TFA	SS / TFA: 12 SF / FA: 5	15	SS: 0.025 SF: 0.015	32
SCO10	SS / TFA and SF / TFA	SS / TFA: 9.5 SF / FA: 5	15	SS: 0.025 SF: 0.015	32
CHCO1	SS / TFA and CS / TFA (1:1 v/v), and SF / FA	SS / TFA: 12 CS / TFA: 2 SF / FA: 7.5	15	0.025	29
CHCO3	SS / TFA and CS / TFA (1:1 v/v), and SF / FA	SS / TFA: 12 CS / TFA: 2 SF / FA: 7.5	15	Blend: 0.05 SF: 0.1	29
CHCO7	SS / TFA and CS / TFA (3:1 v/v) and SF / FA	SS / TFA: 9.5 CS / TFA: 2 SF / FA: 7.5	15	0.025	29
CHCO8	SS / TFA and CS / TFA (3:1 v/v) and SF / FA	SS / TFA: 9.5 CS / TFA: 2 SF / FA: 7.5	15	Blend: 0.05 SF: 0.025	29

Morphological characterization of electrospun films by Scanning Electron Microscopy (SEM)

SEM micrographs and corresponding fibre diameter distribution histograms were used to evaluate the morphological characteristics of the electrospun fibres, providing complementary qualitative and quantitative insights. SEM imaging enabled detailed assessment of surface morphology, fibre continuity, and structural integrity, while diameter measurements quantified fibre uniformity across the investigated samples. As shown in Figs. 2, 3, 4 and 5, SEM images acquired at magnifications of 20 μm and 30 μm revealed fibres that were generally continuous, uniform, and homogeneously distributed, with minimal bead formation or structural defects. These qualitative observations confirm that the electrospinning conditions yielded morphologies suitable for stable fibre performance.

Fibre diameters were measured using Phenom ProSuite software, and the resulting histograms illustrate the corresponding size distributions, reported as mean values with standard deviations. Several formulations exhibited favourable morphological characteristics, including reduced average fibre diameters and narrower distributions, identifying them as the most promising candidates for subsequent functional evaluation.

Inferential statistical analysis confirmed the quantitative relevance of the observed morphological trends. Multi-group comparisons using the Kruskal–Wallis test followed by Dunn's post-hoc analysis demonstrated that both applied voltage and flow rate significantly influenced fibre diameter ($p < 0.05$). In particular, the SS/TFA sys-

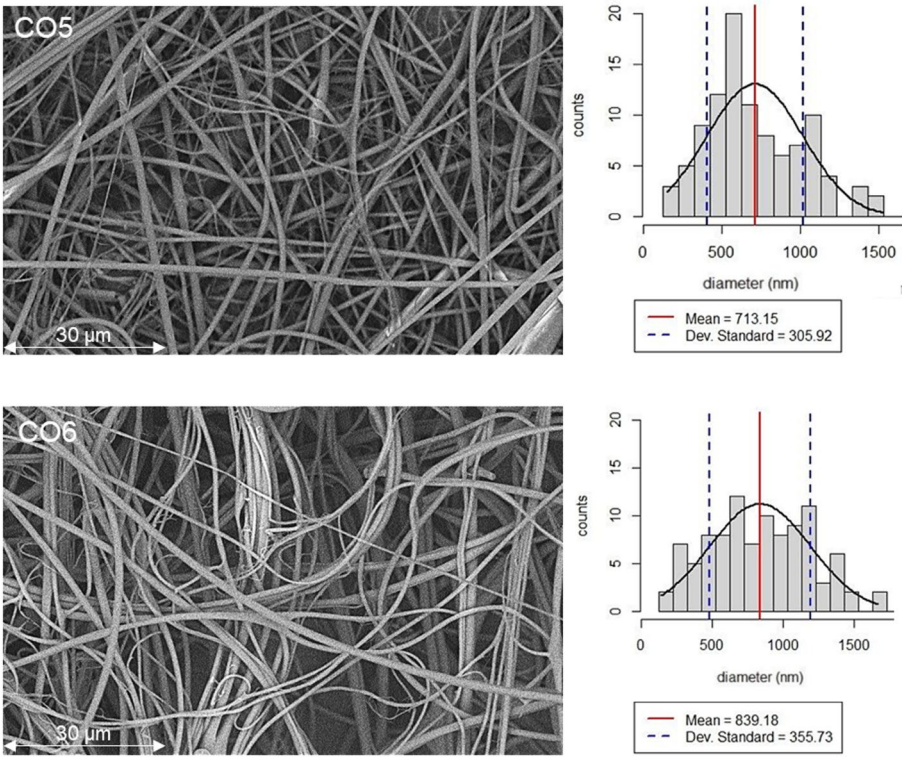

Fig. 2 SEM images of CO5 and CO6 samples, accompanied by histograms illustrating their fibre diameter distribution

tem exhibited a pronounced linear dependence of fibre diameter on applied voltage, as evidenced by rank-based regression analysis ($R^2 = 0.9973$).

The influence of electrospinning configuration was first examined using samples CO5 and CO6, both comprising an SS/TFA shell and an SF/FA core. CO5, fabricated using a single-pump setup, displayed a more uniform fibre distribution with reduced overlap, whereas CO6, produced with a dual-pump system, exhibited increased fibre crowding and overlap. These differences were attributed to minor flow instabilities arising from independently driven solutions. Correspondingly, CO5 showed a lower mean fibre diameter (713.5 ± 305.9 nm) than CO6 (839.2 ± 355.7 nm).

The feasibility of coaxial electrospinning using a single solvent system was evaluated using samples SCO4 and SCO10, in which both SS and SF were dissolved in TFA. Despite the known instability of SF in TFA, both samples yielded structurally consistent fibres. SCO10 exhibited a slightly reduced mean diameter (672.9 ± 299.4 nm) compared to SCO4 (717.9 ± 264.2 nm), accompanied by improved fibre alignment and fewer surface defects. Statistical comparison via Student's *t*-test indicated that reducing the sericin concentration from 12 wt% to 9.5 wt% did not significantly affect fibre diameter ($p = 0.131$), demonstrating that the single-solvent coaxial configuration is relatively insensitive to moderate shell concentration variations.

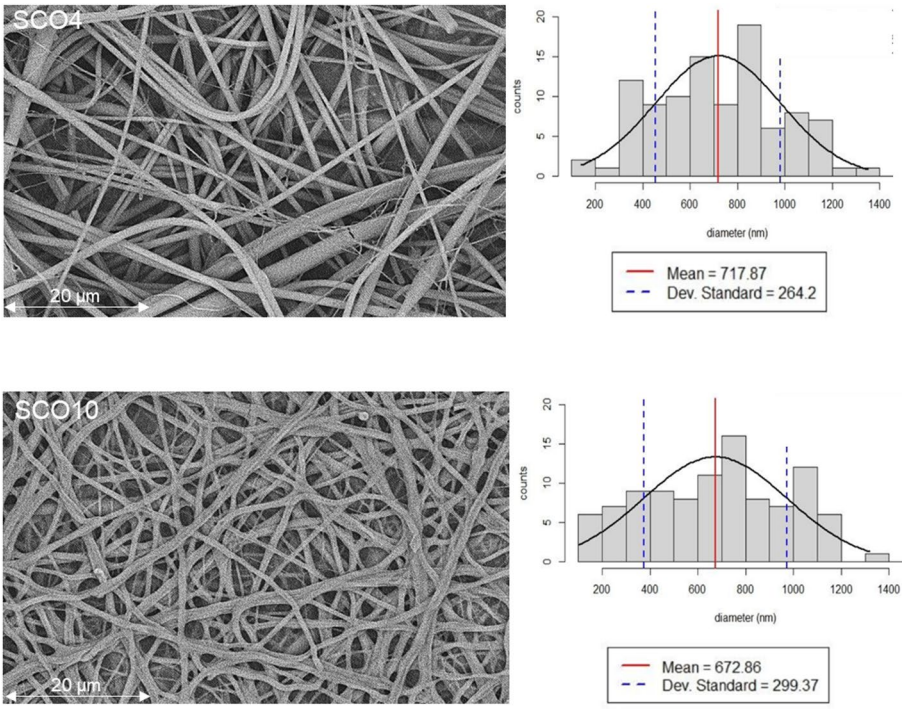

Fig. 3 SEM images of SCO4 and SCO10 samples, accompanied by histograms illustrating their fibre diameter distributions

The effect of chitosan incorporation into the sheath was investigated using samples CHCO1, CHCO3, CHCO7, and CHCO8, all employing an SF/FA core. For equimolar SS: CS blends (1:1 v/v, 12 wt% sericin), CHCO3 exhibited markedly improved morphology and a significantly reduced mean diameter (415.4 ± 194.5 nm) relative to CHCO1 (795.4 ± 253.1 nm), indicating enhanced electrospinning stability. For reduced-viscosity blends (3:1 v/v SS: CS, 9.5 wt% sericin), CHCO7 produced well-defined, uniform fibres with a mean diameter of 450.4 ± 170.5 nm, whereas CHCO8 yielded larger fibres (633.3 ± 219.9 nm).

Kolmogorov–Smirnov analysis revealed that the introduction of chitosan into the sheath significantly altered fibre diameter distributions, resulting in a pronounced reduction in fibre size relative to chitosan-free systems ($p < 0.0001$). However, within SS–CS/TFA blends, increasing chitosan content led to a statistically significant increase in fibre diameter, attributable to elevated solution viscosity arising from strong intermolecular interactions and three-dimensional polymer network formation.

These findings underscore the importance of blend ratio and sericin concentration optimisation in achieving balanced fibre diameter and electrospinning stability.

Table 2 summarizes the composition and mean fibre diameter (± standard deviation) for the eight selected samples, illustrating the combined effects of solvent choice, pump configuration, and polymer blending on fibre morphology and uniformity.

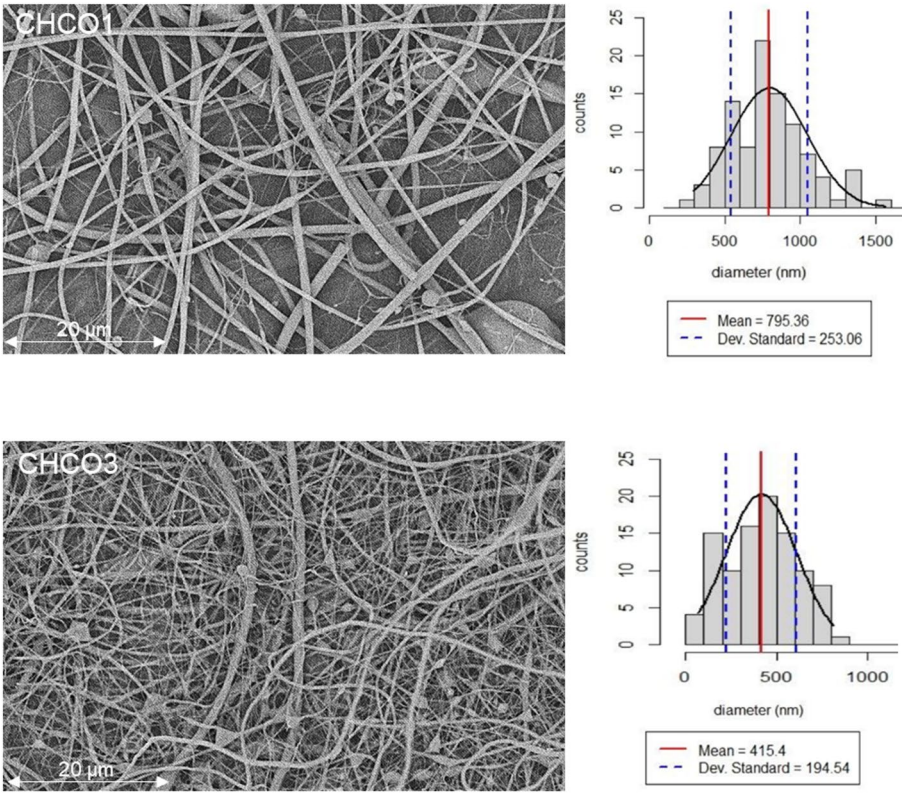

Fig. 4 SEM images of CHCO1 and CHCO3 samples, accompanied by histograms illustrating their fibre diameter distributions

Among all investigated formulations, sample CHCO7 exhibited the most favourable overall fibre morphology, characterized by well-defined, uniform fibres with a comparatively small mean diameter and narrow distribution. Although the SS concentration in CHCO7 (9.5 wt%) was lower than the optimum value identified for pure SS/TFA electrospinning, the incorporation of a limited amount of CS (SS: CS = 3:1 v/v) appeared to improve fibre formation and dimensional uniformity. The reduced diameter of CHCO7 is consistent with the fibre-size-modifying effect of CS discussed in Sect. 3.1, where moderate chitosan incorporation was proposed to promote greater electrostatic jet stretching during electrospinning [31]. This behaviour suggests that, within an appropriate compositional range, CS can positively influence the electrospinning performance of the shell phase. In contrast, formulations containing higher relative amounts of CS (e.g., the 1:1 SS/CS blends) exhibited poorer fibre quality, indicating that excessive viscosity can outweigh any beneficial contribution of chitosan. These results indicate that CHCO7 provided the most favourable balance of fibre quality, dimensional uniformity, and process stability among the investigated formulations, identifying it as the most promising candidate for subsequent functional evaluation.

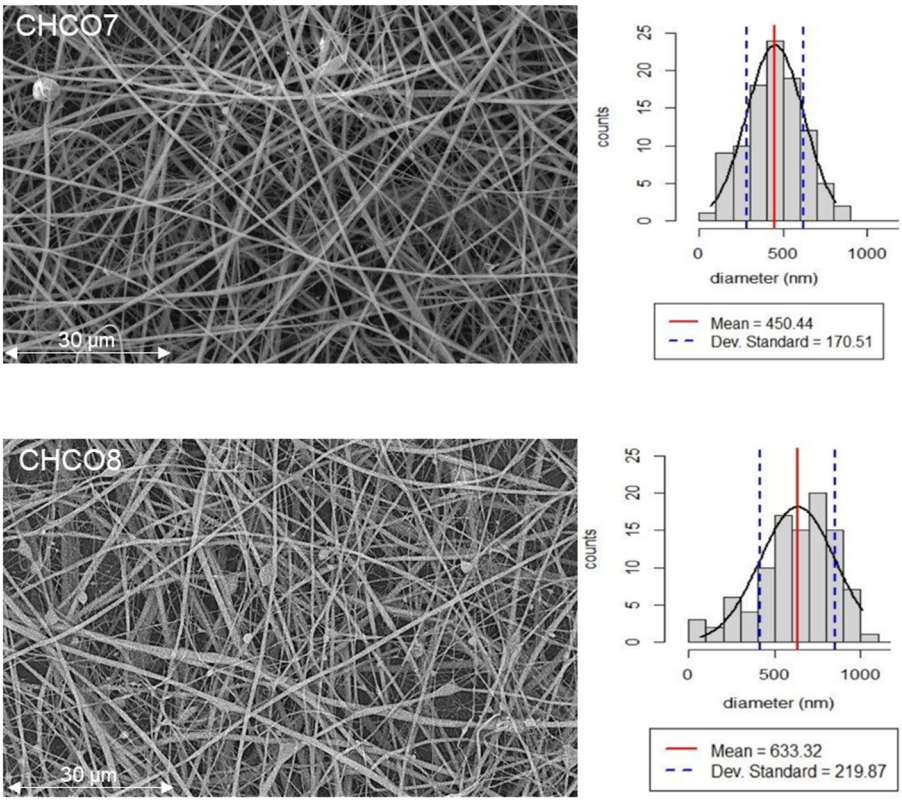

Fig. 5 SEM images of CHCO7 and CHCO8 samples, accompanied by histograms illustrating their fibre diameter distributions

Table 2 Composition and mean fibre diameter (±SD) of the eight best samples

Sample name	Composition	Mean fibre diameter (±SD)
CO5	SS / TFA and SF / FA	713.5 (±305.92)
CO6	SS / TFA and SF / FA	839.18 (±355.73)
SCO4	SS / TFA and SF / TFA	717.87 (±264.2)
SCO10	SS / TFA and SF / TFA	672.86 (±299.37)
CHCO1	SS / TFA and CS / TFA (1:1 v/v), and SF / FA	795.36 (±253.06)
CHCO3	SS / TFA and CS / TFA (1:1 v/v), and SF / FA	415.4 (±194.54)
CHCO7	SS / TFA and CS / TFA (3:1 v/v) and SF / FA	450.44 (±170.51)
CHCO8	SS / TFA and CS / TFA (3:1 v/v) and SF / FA	633.32 (±219.87)

Morphological characterization of electrospun films by Transmission Electron Microscopy (TEM)

To confirm the formation of core-sheath structured fibres, sample CHCO7, identified earlier as the most promising candidate, was electrospun directly onto the copper grid, and the TEM images were acquired. The electrospinning procedure, optimized for this type of deposition, resulted in a dense network of fibres (Fig. 6, A and B), making it challenging to analyse single fibres without artefacts caused by fibre overlap (Fig. 6, C, green arrows). For this reason, quantitative fibre diameter analysis was performed using SEM micrographs, which provided a larger and more representative fibre population for statistical evaluation, whereas TEM was employed primarily to assess the internal core–sheath morphology of the fibres. Nevertheless, some isolated fibres displayed features indicative of a core–sheath architecture: a distinct central core surrounded by a more diffuse outer shell, with a visible interface between them (red arrows in Fig. 6, C and D). In the same image (Fig. 6, C), the fibre on the right shows two different contrasts along its cross-section, suggesting the presence of two distinct materials within a single fibre. To further corroborate this interpretation, additional TEM images, acquired on a sample with SS/TFA in the shell and SF/FA in the core (Fig. 6E and F), similarly reveal a distinct internal core surrounded by a more diffuse shell. In particular, the presence of morphological irregularities, likely due to instabilities in the coaxial electrospinning jet and/or partial degradation during TEM imaging collection, can facilitate the visualization of the two components of the core-sheath fibres. As shown in Fig. 6E, F and a distinct internal fibrillar core is visible, surrounded by a more diffuse external shell structure.

Consistent with previous studies on chitosan-based core–sheath electrospun nanofibers, TEM analysis has been shown to reliably confirm core–sheath architectures through the observation of distinct contrast differences and a visible internal interface arising from density and compositional differences between the core and shell materials [26, 41].

These observations support the successful fabrication of core–sheath fibres by coaxial electrospinning.

Attenuated Total Reflection Fourier Transform Infrared (ATR-FTIR) Spectroscopy

To gain deeper insight into the structural properties of fibres obtained via coaxial electrospinning, the eight best-performing samples were analysed by FTIR. These samples were selected based on their morphological quality, fibre dimensions, and process stability across different experimental conditions. The analysis aimed to identify characteristic functional groups and secondary structures of the biopolymers used. The samples analysed are listed in Table 3.

In Fig. 7, A, the ATR-FTIR absorption spectra of the selected core-sheath fibres are shown between 1800 –1490 cm^{-1}. In this spectral range, the absorption of protein Amide I and II bands is observed alongside a component around 1740 cm^{-1}, which is attributed to the TFA and FA carbonyl group. By comparing these bands, clear distinctions emerged among the samples. To resolve the Amide I components assignable to protein secondary structure in accordance with established literature [42, 43],

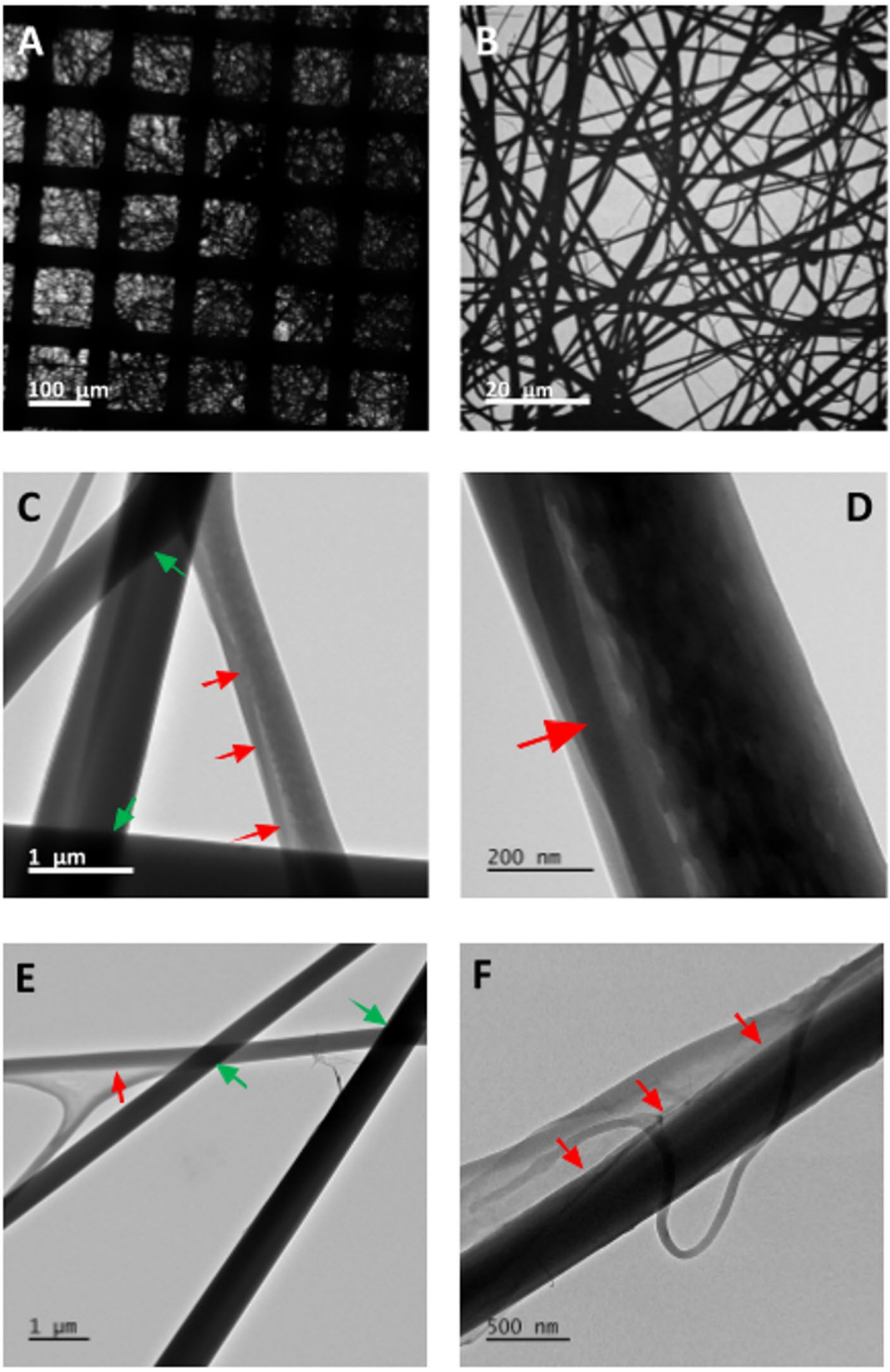

Fig. 6 TEM images of CHCO7 (**A**, **B**, **C**, and **D**), and a sample with SS/TFA in the shell and SF/FA in the core (**E** and **F**). Green arrows indicate overlapping fibres. Red arrows indicate the boundary between the inner and outer parts of core-sheath fibres

Table 3 Samples analysed with their corresponding compositions and applied solvents

Sample name	Composition
CO5, CO6	SS / TFA and SF / FA
SCO4, SCO10	SS / TFA and SF / TFA
CHCO1, CHCO3	SS / TFA and CS / TFA (1:1 v/v), and SF / FA
CHCO7, CHCO8	SS / TFA and CS / TFA (3:1 v/v) and SF / FA

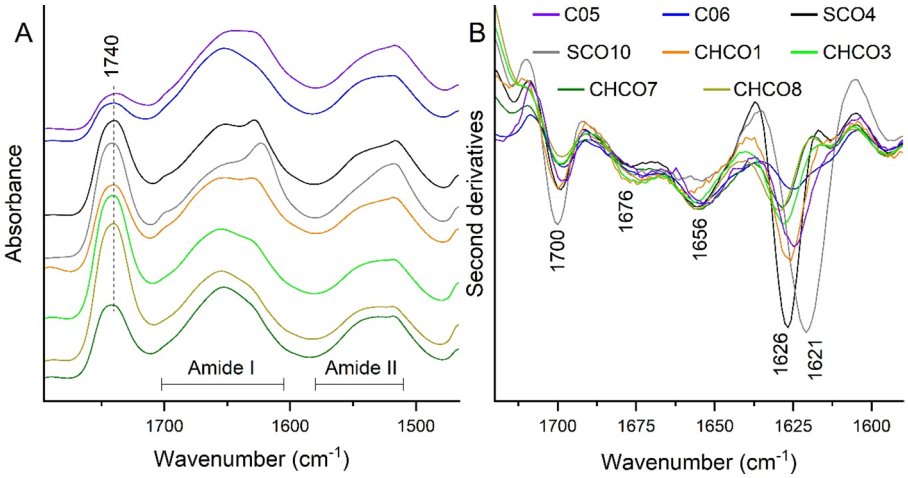

Fig. 7 FTIR analysis of key core-sheath fibres. (**A**) ATR-FTIR absorption spectra of core-sheath fibres between approximately 1800–1490 cm^{-1}. (**B**) Second derivatives of the ATR-FTIR absorption spectra in A) in the Amide I band. The main spectral components have been indicated

a second derivative analysis was performed (Fig. 7, B). In particular, in the Amide I band, β-sheet structures are identified by characteristic peaks around 1620–1627 cm^{-1} and at approximately 1700 cm^{-1}. Moreover, the component around 1656 cm^{-1} is mainly assigned to random coil structures, while that around 1676 cm^{-1} is mainly due to β-turn structures [43].

The CHCO7 and CHCO8 showed almost overlapping spectral profiles in the secondary structure region, but CHCO8 displayed a stronger peak at 1740 cm^{-1}, indicating higher TFA and/or FA residue (Fig. 7, A). This was correlated with the presence of droplets and melted fibre zones in SEM images (see Fig. 5), confirming poor solvent evaporation. In contrast, CHCO7 exhibited better-defined fibres (Fig. 5) and lower residual solvent, making it the most balanced among the CHCO group.

CHCO3 and CHCO1, prepared with a 1:1 SS/CS blend, also showed high solvent retention (Fig. 7, A) and a slightly more intense component around 1676 cm^{-1} (Fig. 7, B) that can also be associated with CS interactions. However, the quality of its fibres was lower, with structural inconsistencies and melting zones. CHCO1 could not be reliably analysed due to poor fibre formation.

The CO5 and CO6 samples (without chitosan) displayed minimal TFA/FA residue (Fig. 7, A), demonstrating excellent solvent evaporation. Notably, CO5 showed a more intense β-sheet peak around 1623 cm^{-1} when compared to CO6, which in turn displayed a broader and lower β-sheet component (Fig. 7, B) among all the analysed

samples. These differences highlight the influence of chitosan on solvent retention and molecular assembly, possibly by increasing solution viscosity and hindering polymer mobility.

Interestingly, SCO4 and SCO10, both made using SF and SS in TFA, showed unexpectedly strong β-sheet peaks, despite TFA's known denaturing effect on fibroin. Notably, the second derivative analysis (Fig. 7, B) discloses a few differences between SCO10 and SCO4. In particular, SCO4 displayed a β-sheet peak at a higher wavenumber (1626 cm^{-1}) compared to SCO10 (1621 cm^{-1}). Furthermore, SCO10 showed a more intense band at 1700 cm^{-1}. Collectively, these spectral characteristics indicate that SCO10 possesses tighter internal fibre structures. This may suggest a synergistic interaction between SS and SF in the same solvent, promoting partial ordering. However, SCO4 and SCO10 samples also trapped significant amounts of solvent, particularly SCO10, caused by large melting zones and droplet formation. In conclusion, FTIR analysis, supported by SEM imaging, enabled the inference of both the chemical composition and structure of the different fibres. Among all, CHCO7 emerged as the most representative sample, combining structural integrity, acceptable solvent content, and evidence of all three biomolecules, thus chosen for subsequent functional testing.

Moisture Vapour Transmission Rate (MVTR) Evaluation

In line with the FTIR analysis, the CHCO7 formulation was identified as the most promising candidate and was therefore selected for moisture regulation assessment. The Moisture Vapour Transmission Rate (MVTR) of CHCO7 electrospun films fabricated for 30 min, 1 h, and 1.5 h was evaluated using steady-state gravimetric analysis. As shown in Fig. 8, the mass of water-filled flasks sealed with each film was monitored at 2-h intervals over a 24-h period under controlled conditions (37 °C,

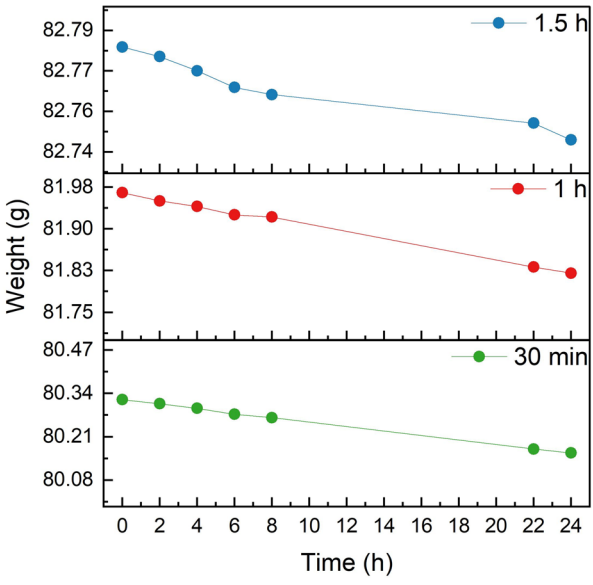

Fig. 8 Trend of the weights of the flasks covered by the films (performed for ES times of 30 min, 1 h, and 1.5 h) as a function of the time elapsed since the first measurement

95% relative humidity). Each deposition time (30 min, 1 h, and 1.5 h) was initially represented by a single film and analysed as a screening experiment to assess the effect of film thickness on moisture transport behaviour. The 30-min and 1-h films exhibited highly linear mass-loss kinetics, with excellent goodness of fit ($R^2 \approx 0.99$). The 30-min film showed a mass-loss rate of -0.00670 g·h^{-1} (95% CI: -0.00690 to -0.00649 g·h^{-1}), while the 1-h film displayed a comparable slope of -0.00601 g·h^{-1} (95% CI: -0.00632 to -0.00570 g·h^{-1}). These results indicate stable and consistent moisture transmission behaviour for both thinner electrospun films.

In contrast, the 1.5-h film exhibited pronounced instability and a substantially reduced mass-loss rate of -0.00143 g·h^{-1} (95% CI: -0.00186 to -0.00101 g·h^{-1}), consistent with its increased thickness and reduced permeability. Although visual inspection suggested a potential outlier at the 22-h time point, robust linear regression using Huber weighting yielded a slope (-0.001435 g·h^{-1}) nearly identical to the ordinary least-squares (OLS) estimate, confirming that the suspected outlier did not meaningfully bias the regression. The OLS model produced an R^2 of 0.937 (adjusted $R^2 = 0.924$), indicating a strong but less stable linear relationship. Notably, the 1.5-h film fractured after approximately 24 h of incubation, likely due to impaired moisture transport, surface water accumulation, and consequent mechanical failure.

For comparative evaluation, the mass-loss rates were normalized to a reference relative humidity of 80%. The resulting MVTR values were 2046.88 g·m^{-2}·day^{-1} for the 30-min film, 1834.39 g·m^{-2}·day^{-1} for the 1-h film, and 428.03 g·m^{-2}·day^{-1} for the 1.5-h film. These results demonstrate that thinner electrospun films exhibit significantly higher vapor permeability, highlighting the strong influence of deposition time and thickness on moisture transport properties. Among the tested configurations, the 30-min CHCO7 film displayed the highest permeability, indicating enhanced breathability associated with reduced fibre accumulation and pore obstruction.

However, films thinner than 30 min of electrospinning time were not mechanically stable enough for use. To assess reproducibility, three additional 30-min ES films (S1, S2, S3) were prepared and tested alongside the original (S0) under identical conditions. Weight loss trends were consistent across all samples, as shown in Fig. 9. The precision and reproducibility of the experimental setup were validated through a one-way ANOVA performed on four independent measurement sets (S0–S3) of the optimized 30-min films, which revealed no statistically significant inter-set differences ($p = 0.8248$). Furthermore, coefficients of variation at each time point remained below 0.04%, confirming minimal dispersion and high metrological reliability throughout the 24-h measurement period.

In conclusion, the 30-minute electrospun film exhibited the highest vapor permeability while maintaining structural integrity and experimental repeatability. The results highlight the strong influence of deposition time on moisture transport behaviour and fibre packing density. Among the tested configurations, the 30-minute film provided the most favourable balance between permeability and structural stability under the investigated processing conditions. Moreover, the electrospinning process demonstrated robustness and reproducibility across multiple preparations, confirming the reliability of the selected parameters and solution formulation.

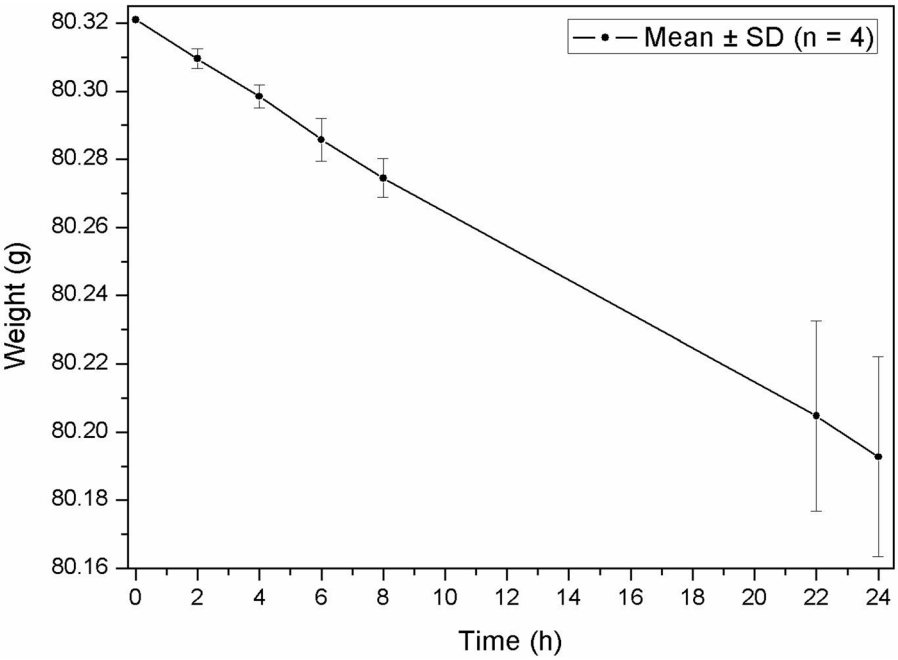

Fig. 9 Weight variation during the moisture transport test as a function of time. Data are presented as mean ± standard deviation of four independent samples ($n = 4$)

Conclusion

In this study, coaxial electrospinning was systematically investigated as a strategy for fabricating nanofibrous scaffolds based on SF, SS, and CS. The central hypothesis was that a core–sheath architecture comprising an SF core and an SS–CS sheath could combine the mechanical stability of fibroin with the tunable surface and structural characteristics imparted by sericin and chitosan. Through a stepwise experimental approach progressing from single-material electrospinning to increasingly complex coaxial configurations, stable processing windows were identified, and representative formulations were successfully fabricated with high reproducibility.

A key innovation of this work lies in the integration of three naturally derived biopolymers within a single coaxial electrospun fibre system while systematically establishing the processing parameters required to obtain stable core–sheath structures. The study further demonstrates the potential valorisation of sericin, a silk industry by-product, as a functional component of advanced electrospun materials. In particular, the incorporation of chitosan into the sericin-based sheath enabled modulation of fibre morphology and electrospinning performance through compositional tuning.

Morphological characterisation by SEM demonstrated that fibre diameter, uniformity, and structural integrity are strongly governed by solvent choice, electrospinning configuration, and sheath composition. In particular, incorporation of chitosan into the sericin-based sheath significantly influenced jet stability and fibre morphology. Sericin-rich SS blends (3:1 v/v) produced more uniform fibres with reduced

diameter dispersion compared with equimolar blends, reflecting an optimal balance between charge density and solution viscosity. These trends were supported by robust statistical analysis, confirming the dominant role of processing parameters such as voltage, flow rate, and blend composition in controlling fibre dimensions. Based on these criteria, CHCO7 emerged as the most balanced formulation. Under optimised conditions, CHCO7 exhibited well-defined, continuous fibres with a comparatively small mean diameter and narrow distribution, indicating enhanced electrospinning stability and process control.

TEM provided further evidence for the successful formation of a core–sheath architecture in CHCO7, while FTIR spectroscopy confirmed the coexistence of SF, SS, and CS within the fibres and revealed composition-dependent differences in molecular organisation and residual solvent retention. Compared with the other investigated formulations, CHCO7 exhibited a favourable balance between structural integrity and reduced solvent-associated spectral features, consistent with its superior morphological stability.

Functional assessment through MVTR measurements demonstrated that moisture transport is strongly dependent on electrospun film thickness and structural stability. Thinner electrospun mats displayed higher and more stable vapour transmission rates, whereas thicker films exhibited reduced permeability and, in some cases, mechanical instability during prolonged exposure to high humidity. When normalised to a reference relative humidity of 80%, films produced with shorter electrospinning durations exhibited substantially higher permeability, underscoring the importance of thickness control in tuning moisture transport behaviour without compromising structural integrity or reproducibility.

These findings are consistent with previous studies reporting the strong influence of polymer composition and electrospinning parameters on fibre morphology in silk- and chitosan-based electrospun systems. However, the present work extends existing knowledge by demonstrating the successful fabrication and characterization of a multi-component SF/SS–CS core–sheath architecture and by systematically establishing the processing conditions required to obtain stable fibres from this complex biopolymer combination.

The experimental results support the original hypothesis by demonstrating that appropriate selection of sheath composition and electrospinning conditions enabled the successful fabrication of stable SF/SS–CS core–sheath fibres with tunable morphological characteristics and moisture vapour transport properties.

Overall, this work establishes the feasibility of producing SF/SS–CS core–sheath nanofibrous membranes with controlled morphology, composition, and moisture transport properties through systematic optimisation of electrospinning parameters, while establishing process–structure–property relationships within this multi-component biopolymer system. Future studies should include systematic measurements of solution viscosity, conductivity, and surface tension to establish quantitative relationships between solution properties and fibre morphology. In addition, biological performance, degradation behaviour, long-term environmental stability, and the development of greener solvent systems remain important directions for future investigation. By demonstrating how spatial separation and compositional tuning can be achieved within a single electrospun fibre system, this work provides a statistically

supported foundation for further optimisation and advanced materials development based on silk-derived core–sheath architectures.

Supplementary Information The online version contains supplementary material available at https://doi.org/10.1007/s00289-026-06562-8.

Acknowledgements We acknowledge the Circular Economy Lab for Life Sciences-CELLS within the MUSA–Multilayered Urban Sustainability Action–project, funded by the European Union–NextGeneration EU, under the National Recovery and Resilience Plan (NRRP) Mission 4 Component 2 Investment Line 1.5: Strengthening of research structures and creation of R&D "innovation ecosystems", set up of "territorial leaders in R&D". This study has received funding from the European Union's Horizon Europe Research and Innovation Program under grant agreement No. 101070167 and from Fondazione Cariplo under the project RITESSERE No. 2022-0529.

Author contributions Rony Aad: Conceptualisation, Methodology, Investigation, Data curation, Formal analysis, Writing–original draft, review & editing, Visualisation. Andrea Hejdová: Data curation, Writing–original draft, review & editing, Visualisation. Ivana Dragojlov: Methodology, Writing–original draft, Visualisation. Davide Iaconianni: Investigation, Data curation, Formal analysis, Writing- original draft. Simone Mariuzzo: Investigation, Data curation, Formal analysis, Writing- original draft. Diletta Ami: Investigation, Data curation, Formal analysis, Writing- original draft, Visualisation. Antonino Natalello: Data curation, Formal analysis, Writing- original draft, review & editing, Visualisation. Simone Vesentini: Conceptualisation, Supervision, Writing – original draft, reviewing, and editing, Resources.

Funding Open access funding provided by Politecnico di Milano within the CRUI-CARE Agreement.

Data availability All data supporting the findings of this study are provided in the Supporting Information. This includes the raw fibre diameter datasets ($N = 100$ per selected sample) supplied as an Excel file. Additional datasets generated during this study are available from the corresponding author upon reasonable request.

Declarations

Competing interests The authors declare no competing interests.

References

1. Persano L, Camposeo A, Tekmen C, Pisignano D (2013) Industrial Upscaling of Electrospinning and Applications of Polymer Nanofibers: A Review. Macromol Mater Eng 298:504–520. https://doi.org/10.1002/mame.201200290
2. Agarwal S, Wendorff JH, Greiner A (2008) Use of Electrospinning Technique for Biomedical Applications. Polymer 49:5603–5621. https://doi.org/10.1016/j.polymer.2008.09.014
3. Khan J, Khan A, Khan MQ, Khan H (2024) Applications of Co-Axial Electrospinning in the Biomedical Field. Next Mater 3:100138. https://doi.org/10.1016/j.nxmate.2024.100138

4. Dong R, Gong W, Guo Q, Liu H, Yu D-G (2024) Synergistic Effects of Radical Distributions of Soluble and Insoluble Polymers within Electrospun Nanofibers for an Extending Release of Ferulic Acid. Polymers 16(2614). https://doi.org/10.3390/polym16182614
5. Chen Y, Gong W, Zhang Z, Zhou J, Yu D-G, Yi T (2024) Reverse Gradient Distributions of Drug and Polymer Molecules Within Electrospun Core–Shell Nanofibers for Sustained Release. Int J Mol Sci 25(9524). https://doi.org/10.3390/ijms25179524
6. Wang P, He W, Zhou J, Zhang Z, Feng J, Liu Y, Yu D-G (2026) One-Step Batch Fabrication of Znco ZIFs@TiO2 Nanofibers via Modified Triaxial Electrospinning for Enhanced Photocatalytic Antibiotic Degradation through Peroxymonosulfate Activation. Chem Eng J 536:176198. https://doi.org/10.1016/j.cej.2026.176198
7. Cheng H, Yang X, Che X, Yang M, Zhai G (2018) Biomedical Application and Controlled Drug Release of Electrospun Fibrous Materials. Mater Sci Engineering: C 90:750–763. https://doi.org/10.1016/j.msec.2018.05.007
8. Greiner A, Wendorff JH, Yarin AL, Zussman E (2006) Biohybrid Nanosystems with Polymer Nanofibers and Nanotubes. Appl Microbiol Biotechnol 71:387–393. https://doi.org/10.1007/s00253-006-0356-z
9. Li D, Xia Y (2004) Direct Fabrication of Composite and Ceramic Hollow Nanofibers by Electrospinning. Nano Lett 4:933–938. https://doi.org/10.1021/nl049590f
10. Moghe AK, Gupta BS (2008) Co-axial Electrospinning for Nanofiber Structures: Preparation and Applications. Polym Rev 48:353–377. https://doi.org/10.1080/15583720802022257
11. Elahi MF, Lu W (2013) Core-Shell Fibers for Biomedical Applications - A Review. J Bioeng Biomed Sci 3. https://doi.org/10.4172/2155-9538.1000121
12. Wei Z, Zhang Q, Peng M, Wang X, Long S, Yang J (2014) Preparation and Drug Delivery Study of Electrospun Hollow PES Ultrafine Fibers with a Multilayer Wall. Colloid Polym Sci 292:1339–1345. https://doi.org/10.1007/s00396-014-3187-y
13. Polak M, Uma Thanu Krishnan Neela N, Berniak K, Knapczyk-Korczak J, Marzec MM, Stachewicz U (2026) Comparative Physicochemical Characterization of Electrospun PCL, PLLA, and PLCL Scaffolds and Cell Responses for Tissue Engineering Applications. Macromolecular Bioscience 26:e202500564. https://doi.org/10.1002/mabi.202500564
14. Zhang W, Wang Q, Yi W, Wang H, Yu D-G, Yi T (2026) Electrospun PLA/PVP K90 Biphasic-Release Sublingual Film for Motion Sickness Treatment. Biomolecules 16(363). https://doi.org/10.3390/biom16030363
15. Zhou J, Xue F, Xu L, Liao F, Yu D-G, Ge R (2026) Comparative Study of Bio-Based and Synthetic Phase Change Materials Functionalized Coaxial Fibers for Photothermal-Controlled Drug Delivery. Biomaterials Adv 184:214808. https://doi.org/10.1016/j.bioadv.2026.214808
16. Qi Y, Wang H, Wei K, Yang Y, Zheng R-Y, Kim IS, Zhang K-Q (2017) A Review of Structure Construction of Silk Fibroin Biomaterials from Single Structures to Multi-Level Structures. Int J Mol Sci 18(237). https://doi.org/10.3390/ijms18030237
17. Chen K, Li Y, Li Y, Pan W, Tan G (2023) Silk Fibroin Combined with Electrospinning as a Promising Strategy for Tissue Regeneration. Macromol Biosci 23:e2200380. https://doi.org/10.1002/mabi.202200380
18. Ma L, Dong W, Lai E, Wang J (2024) Silk Fibroin-Based Scaffolds for Tissue Engineering. Front Bioeng Biotechnol 12. https://doi.org/10.3389/fbioe.2024.1381838
19. Aad R, Dragojlov I, Vesentini S (2024) Sericin Protein: Structure, Properties, and Applications. J Funct Biomater 15(322). https://doi.org/10.3390/jfb15110322
20. Reddy R, Jiang Q, Aramwit P, Reddy N (2021) Litter to Leaf: The Unexplored Potential of Silk Byproducts. Trends Biotechnol 39:706–718. https://doi.org/10.1016/j.tibtech.2020.11.001
21. Kunz RI, Brancalhão RMC, Ribeiro LDFC, Natali MRM (2016) Silkworm Sericin: Properties and Biomedical Applications. BioMed Research International 2016, pp 1–19. https://doi.org/10.1155/2016/8175701
22. Karthick SA, Manjari K, Devi MG (2023) Biocompatible and Bioactive PVA/Sericin/Chitosan Nanofibrous Wound Dressing Matrix. Appl Surf Sci Adv 13:100362. https://doi.org/10.1016/j.apsadv.2022.100362
23. Gundhavi Devi M, Arun Karthick S (2024) Fabrication of Chitosan/Sericin/Polyvinyl Alcohol Nanofiber with Silver Nanoparticles for Wound Dressing Applications. Polym Eng Sci 64:4128–4143. https://doi.org/10.1002/pen.26837

24. Zhao R, Li X, Sun B, Zhang Y, Zhang D, Tang Z, Chen X, Wang C (2014) Electrospun Chitosan/Sericin Composite Nanofibers with Antibacterial Property as Potential Wound Dressings. Int J Biol Macromol 68:92–97. https://doi.org/10.1016/j.ijbiomac.2014.04.029
25. Mosallanezhad P, Rajabifar N, Rostami A, Ahmadi Z, Taghdimi R, Nazockdast H (2025) Preparation and Structural Analyses of Antimicrobial Core-Shell Chitosan-Polycaprolactone Nanofibers for Controlled Curcumin Release. Colloids Surf A 716:136736. https://doi.org/10.1016/j.colsurfa.2025.136736
26. Ghazalian M, Afshar S, Rostami A, Rashedi S, Bahrami SH (2022) Fabrication and Characterization of Chitosan-Polycaprolactone Core-Shell Nanofibers Containing Tetracycline Hydrochloride. Colloids Surf A 636:128163. https://doi.org/10.1016/j.colsurfa.2021.128163
27. Sun W, Gregory DA, Tomeh MA, Zhao X (2021) Silk Fibroin as a Functional Biomaterial for Tissue Engineering. Int J Mol Sci 22(1499). https://doi.org/10.3390/ijms22031499
28. Qi Z, Hu Z, Tan G, Chen Y, Liu Y, Lu S (2026) Understanding Solid-State Structural Transitions and Stability of Silk Fibroin from a Bound Water Perspective. Biomacromolecules 27:3772–3786. https://doi.org/10.1021/acs.biomac.6c00256
29. Naito A, Okushita K, Aoki A, Asakura T (2024) Chain-Folded Lamellar Stacking Structure of the Crystalline Fraction of Bombyx Mori Silk Fibroin with Silk II Form Studied by 2D 13 C– 13 C Homonuclear Correlation NMR Spectroscopy. J. Phys. Chem. B 128:8459–8468. https://doi.org/10.1021/acs.jpcb.4c03716
30. Aad R, Leuzzi L, Mandelli S, Cipolla L, Vesentini S (2025) Exploring the Chemical Reactivity and Functionalization of Sericin for Advanced Applications. Next Mater 9:101289. https://doi.org/10.1016/j.nxmate.2025.101289
31. Park WH, Jeong L, Yoo DI, Hudson S (2004) Effect of Chitosan on Morphology and Conformation of Electrospun Silk Fibroin Nanofibers. Polymer 45:7151–7157. https://doi.org/10.1016/j.polymer.2004.08.045
32. Rajkhowa R, Levin B, Redmond SL, Li LH, Wang L, Kanwar JR, Atlas MD, Wang X (2011) Structure and Properties of Biomedical Films Prepared from Aqueous and Acidic Silk Fibroin Solutions. J Biomed. Mater. Res. 97A:37–45. https://doi.org/10.1002/jbm.a.33021
33. Dragojlov I, Aad R, Ami D, Mangiagalli M, Natalello A, Vesentini S (2025) Silk Sericin-Based Electrospun Nanofibers Forming Films for Cosmetic Applications: Preparation, Characterization, and Efficacy Evaluation. Molecules 30(715). https://doi.org/10.3390/molecules30030715
34. Geng X, Kwon O, Jang J (2005) Electrospinning of Chitosan Dissolved in Concentrated Acetic Acid Solution. Biomaterials 26:5427–5432. https://doi.org/10.1016/j.biomaterials.2005.01.066
35. De Vrieze S, Van Camp T, Nelvig A, Hagström B, Westbroek P, De Clerck K (2009) The Effect of Temperature and Humidity on Electrospinning. J Mater Sci 44:1357–1362. https://doi.org/10.1007/s10853-008-3010-6
36. Ami D, Mereghetti P, Foli A, Tasaki M, Milani P, Nuvolone M, Palladini G, Merlini G, Lavatelli F, Natalello A (2019) ATR-FTIR Spectroscopy Supported by Multivariate Analysis for the Characterization of Adipose Tissue Aspirates from Patients Affected by Systemic Amyloidosis. Anal. Chem 91:2894–2900. https://doi.org/10.1021/acs.analchem.8b05008
37. Bassan P, Sachdeva A, Kohler A, Hughes C, Henderson A, Boyle J, Shanks JH, Brown M, Clarke NW, Gardner P (2012) FTIR Microscopy of Biological Cells and Tissue: Data Analysis Using Resonant Mie Scattering (RMieS) EMSC Algorithm. Analyst 137:1370. https://doi.org/10.1039/c2an16088a
38. Chen J-P, Chen S-H, Lai G-J (2012) Preparation and Characterization of Biomimetic Silk Fibroin/Chitosan Composite Nanofibers by Electrospinning for Osteoblasts Culture. Nanoscale Res Lett 7:170. https://doi.org/10.1186/1556-276X-7-170
39. Marelli B, Alessandrino A, Farè S, Freddi G, Mantovani D, Tanzi MC (2010) Compliant Electrospun Silk Fibroin Tubes for Small Vessel Bypass Grafting. Acta Biomaterialia 6:4019–4026. https://doi.org/10.1016/j.actbio.2010.05.008
40. Li S, Li Y, Zhang X, Jiang D, Kong L (2026) Electrospinning of Chitosan-Based Nanofibers: Innovations in Fabrication and Applications. Journal of Agriculture and Food Research 25:102599. https://doi.org/10.1016/j.jafr.2025.102599
41. Nguyen TTT, Chung OH, Park JS (2011) Coaxial Electrospun Poly(Lactic Acid)/Chitosan (Core/Shell) Composite Nanofibers and Their Antibacterial Activity. Carbohydrate Polymers 86:1799–1806. https://doi.org/10.1016/j.carbpol.2011.07.014
42. Barth A (2007) Infrared Spectroscopy of Proteins. Biochimica et Biophysica Acta (BBA). Bioenergetics 1767:1073–1101. https://doi.org/10.1016/j.bbabio.2007.06.004

43. Ami D, Natalello A (2022) Characterization of the Conformational Properties of Soluble and Insoluble Proteins by Fourier Transform Infrared Spectroscopy. In Insoluble Proteins; Garcia Fruitós, E., Arís Giralt, A., Eds.; Methods in Molecular Biology; Springer US: New York, NY. 2406:439–454. ISBN 978-1-0716-1858-5.

Authors and Affiliations

Rony Aad[1] · Andrea Hejdová[1] · Ivana Dragojlov[1] · Davide Iaconianni[1] · Simone Mariuzzo[1] · Diletta Ami[2] · Antonino Natalello[2] · Simone Vesentini[1]

✉ Simone Vesentini
simone.vesentini@polimi.it

[1] Department of Electronics, Information, and Bioengineering, Politecnico di Milano, Milan 20133, Italy

[2] Department of Biotechnology and Biosciences, University of Milano-Bicocca, Milano 20126, Italy